

Hierarchical Defective Fe_{3-x}C@C Hollow Microsphere Enables Fast and Long-Lasting Lithium–Sulfur Batteries

Yongguang Zhang, Gaoran Li, Jiayi Wang, Guoliang Cui, Xiaoling Wei, Lingling Shui, Krzysztof Kempa, Guofu Zhou, Xin Wang,* and Zhongwei Chen*

Lithium–sulfur (Li–S) batteries present one of the most promising energy storage systems owing to their high energy density and low cost. However, the commercialization of Li–S batteries is still hindered by several technical issues; the notorious polysulfide shuttling and sluggish sulfur conversion kinetics. In this work, unique hierarchical Fe_{3-x}C@C hollow microspheres as an advanced sulfur immobilizer and promoter for enabling high-efficiency Li–S batteries is developed. The porous hollow architecture not only accommodates the volume variation upon the lithiation–delithiation processes, but also exposes vast active interfaces for facilitated sulfur redox reactions. Meanwhile, the mesoporous carbon coating establishes a highly conductive network for fast electron transportation. More importantly, the defective Fe_{3-x}C nanosized subunits impose strong LiPS adsorption and catalyzation, enabling fast and durable sulfur electrochemistry. Attributed to these structural superiorities, the obtained sulfur electrodes exhibit excellent electrochemical performance, i.e., high areal capacity of 5.6 mAh cm⁻², rate capability up to 5 C, and stable cycling over 1000 cycles with a low capacity fading rate of 0.04% per cycle at 1 C, demonstrating great promise in the development of practical Li–S batteries.

1. Introduction

Lithium–sulfur (Li–S) batteries have been emerging as one of the most promising energy storage systems owing to their high energy density (2600 Wh kg⁻¹), low cost and environmental compatibility compared with conventional lithium-ion batteries (LIBs).^[1–3] Despite these attractive advantages, the development of commercially viable Li–S batteries is still seriously hindered by several technical problems, including the intrinsically low conductivity of sulfur, the dissolution and shuttling behaviors of lithium polysulfide (LiPS) intermediates, the large volume change (≈80%) of sulfur during charge–discharge process, and the tardy LiPS conversion kinetics, which result in poor cyclic stability and rate capability.^[4–9]

Porous carbon materials have been recognized as excellent sulfur hosts to improve the Li–S battery performance attributed to their high electronic conductivity and large surface area.^[10–15] However,

the nonpolar carbon materials exhibit poor affinity toward LiPS, resulting in unsatisfied LiPS shuttle inhibition.^[16–18] In view of this, polar inorganics such as metal oxides/sulfides have been developed as sulfur host to take advantages of their stronger chemical interactions with LiPS. However, these materials suffer from relatively poor ionic/electronic conductivity and limited surface area with a resultant low-efficiency sulfur redox conversion.^[19–25] Recently, Fe₃C has been reported with strong electrocatalytic activity in oxygen reduction reaction (ORR), which inspires its application as sulfur promoter to facilitate the LiPS conversion process considering the similar redox mechanism between sulfur and oxygen electrochemistry. In addition, defect engineering has been revealed with good capability of altering the physicochemical and electronic structures for enhanced adsorptive and catalytic features, which offers a promising approach toward favorable sulfur host materials for improved Li–S battery chemistry.^[26,27]

Given this, we here developed the unique hierarchical Fe_{3-x}C@C hollow microspheres with enriched Fe-vacancies and mesoporous carbon coating as advanced sulfur host materials in Li–S batteries. The experimental and computational results evidentially revealed the strong sulfur immobilization by the Fe-deficient Fe_{3-x}C as well as its good catalytic capability for

Prof. Y. Zhang, J. Wang, G. Cui, X. Wei, Prof. L. Shui, Prof. K. Kempa, Prof. G. Zhou, Prof. X. Wang, Prof. Z. Chen
School of Information and Optoelectronic Science and Engineering & South China Academy of Advanced Optoelectronics
South China Normal University
Guangzhou 510006, China
E-mail: wangxin@scnu.edu.cn; zhwchen@uwaterloo.ca

Prof. Y. Zhang, G. Cui
School of Materials Science and Engineering
Tianjin Key Laboratory of Materials Laminating Fabrication and Interface Control Technology
Hebei University of Technology
Tianjin 300130, China

Dr. G. Li, Prof. Z. Chen
Department of Chemical Engineering
University of Waterloo
Waterloo, ON N2L 3G1, Canada

Prof. K. Kempa
Department of Physics
Boston College
Chestnut Hill, MA 02467, USA

 The ORCID identification number(s) for the author(s) of this article can be found under <https://doi.org/10.1002/adfm.202001165>.

DOI: 10.1002/adfm.202001165

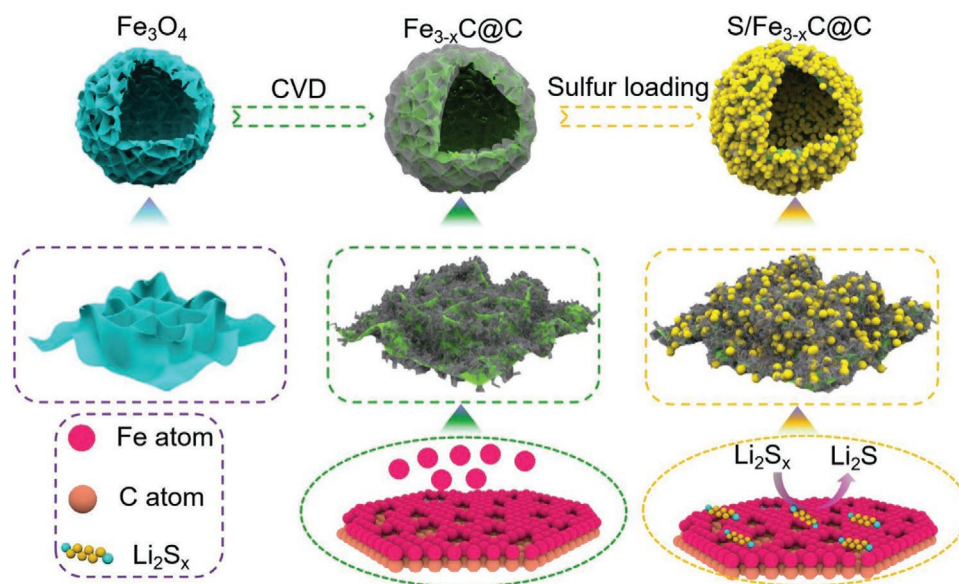


Figure 1. Schematic illustration of the synthesis of the S/Fe_{3-x}C@C.

LiPS conversion, which enabled effective shuttle inhibition and fast sulfur redox kinetics. Meanwhile, the hollow and porous architecture not only facilitates the efficient exposure of active interfaces, but also establishes favorable electron/ion transfer highways in collaboration with the surface carbon coating, further contributing to the fast and stable sulfur electrochemistry. Attributed to these structural features, the Fe_{3-x}C@C-based sulfur electrodes exhibit excellent Li-S performance, i.e., high areal capacity of 5.6 mAh cm⁻², superb rate capability up to 5 C, and high capacity retention of 60% over 1000 cycles, holding a great promise in the development of high-performance Li-S batteries for practical applications.

2. Results and Discussion

Figure 1 schematically illustrates the synthetic route of S/Fe_{3-x}C@C composite. The porous Fe₃O₄ hollow microsphere was prepared by simple hydrothermal process with a subsequent calcination (see details in Experimental section). The following chemical vapor deposition (CVD) was applied to convert the Fe₃O₄ into Fe₃C while depositing a carbon coating on the surface (denoted as Fe_{3-x}C@C hollow microspheres). After sulfur loading, the S/Fe_{3-x}C@C composite was obtained and used as the cathode materials for further electrochemical evaluations.

The morphology and microstructure of the obtained Fe₃O₄ were characterized by the field emission scanning electron microscopy (SEM) and transmission electron microscopy (TEM) as shown in Figure S1 (Supporting Information). The Fe₃O₄ shows clear hollow microsphere morphology with uniform size of around 500 nm. Meanwhile, the nanosheet-like assembly of ultrafine Fe₃O₄ nanoparticles can be observed on the microsphere surface. After the CVD treatment at 500 °C, the Fe_{3-x}C@C-500 hollow microspheres can be obtained, which well maintain the parent microspheric morphology

of Fe₃O₄. **Figure 2a,b** show the SEM images of the porous Fe_{3-x}C@C-500 microspheres in good size uniformity (average size of around 580 nm, Figure S2, Supporting Information). The EDX elemental mapping reveals the uniform distribution of Fe and C in the obtained Fe_{3-x}C@C-500 microspheres (Figure 2c). Figure 2d shows the typical TEM image of the Fe_{3-x}C@C-500 hollow microsphere, which confirms its hierarchical architecture and large hollow interior. Moreover, the mesoporous carbon coating can be observed, which supports the Fe_{3-x}C nanosized subunits to ensure a good electron/ion transfer (Figure 2e). The inverse fast Fourier transformation (IFFT) image on the selected area of the Fe_{3-x}C nanoparticle reveals the lattice fringe with an interplanar spacing of 0.201 nm (Figure 2f,g), corresponding to the (031) plane of orthorhombic Fe₃C.^[27] Notably, relatively disordered lattice moieties can be noticed (yellow frame), signifying the existence of defective structures. Consistently, abundant lattice defects can be also observed in the high-resolution TEM (HRTEM) image of Fe_{3-x}C nanoparticle (Figure 2h), which could be associated with the Fe vacancies. In addition, the TEM elemental mapping further demonstrates the uniform distribution of C, Fe, and O in the obtained composite materials (Figure 2i-l). For comparisons, Fe_{3-x}C@C composites were also prepared under different temperatures (denoted as Fe_{3-x}C@C-400 and Fe_{3-x}C@C-600) with their SEM and TEM images displayed in Figure S3 (Supporting Information). It can be perceived that the spherical and hollow structure can be well maintained in spite of the temperature variation. While the Fe_{3-x}C@C-400 seems morphologically similar to Fe_{3-x}C@C-500 (Figure S3a-c, Supporting Information), the partial structural collapse and severe agglomeration can be clearly observed in Fe_{3-x}C@C-600 ascribed to the uncontrolled size growth of Fe_{3-x}C particles under the excessively high annealing temperature (Figure S3e,f, Supporting Information).

The XRD peaks in Figure S4 (Supporting Information) well matches the cubic Fe₃O₄ phase (JCPDS No. 65-3107), indicating

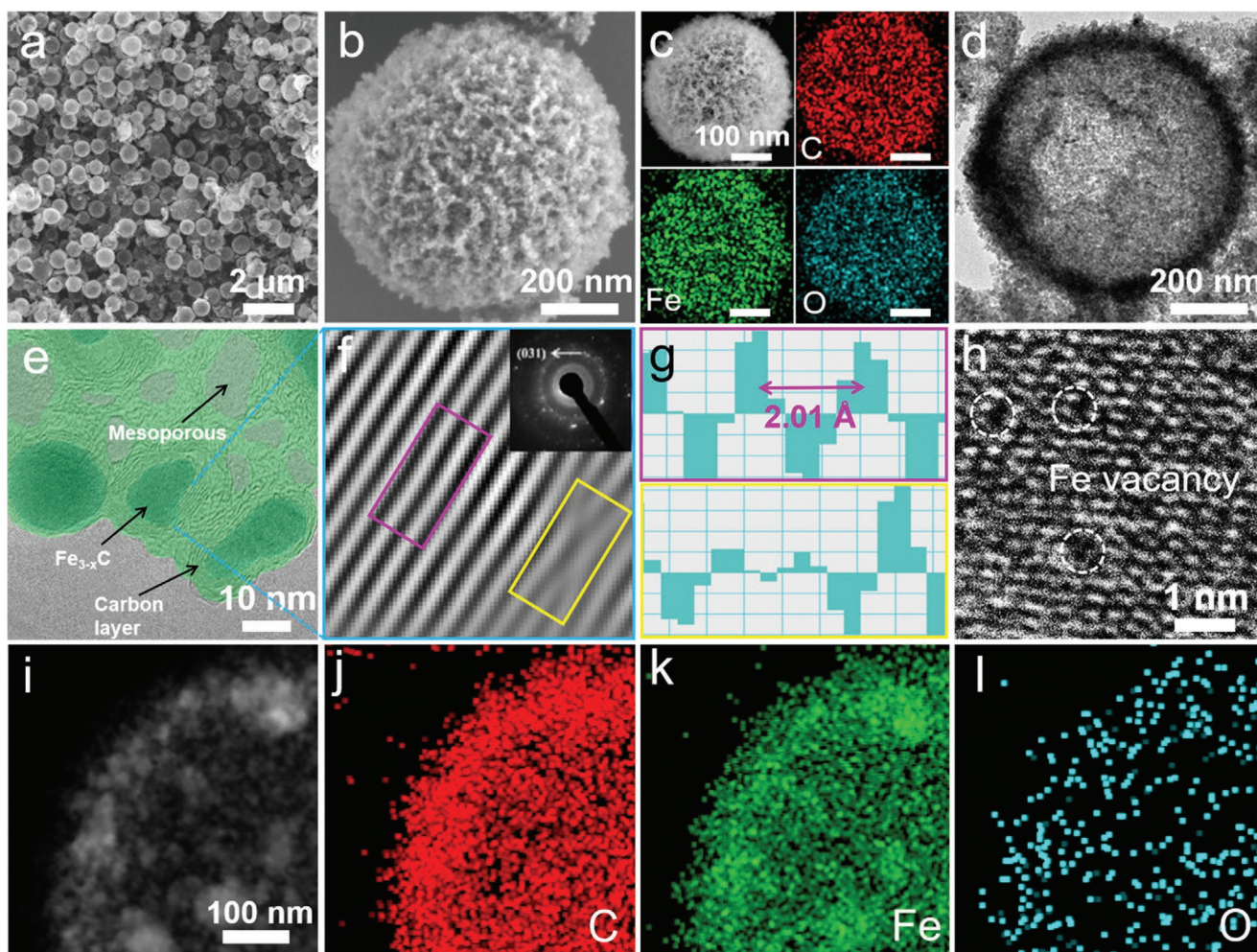


Figure 2. a,b) SEM images and c) element mapping of $\text{Fe}_{3-x}\text{C}@C-500$; d,e) TEM images of $\text{Fe}_{3-x}\text{C}@C-500$ hollow microspheres; f) IFFT and SAED (inset) patterns of selected area; g) lattice spacing profiles at selected areas; h) HRTEM image of $\text{Fe}_{3-x}\text{C}@C-500$; i-l) high-magnification elemental mapping of $\text{Fe}_{3-x}\text{C}@C-500$.

the successful preparation of Fe_3O_4 with a good purity. The XRD patterns of different $\text{Fe}_{3-x}\text{C}@C$ microspheres were also collected as presented in Figure 3a. After the CVD treatment, the Fe_3O_4 microspheres were successfully converted into orthorhombic Fe_3C as verified by the clear diffraction peaks well-indexed to PDF#35-0772. The broad peak at around 26° can be attributed to the carbon coating. It can be noticed that this carbon peak is significantly weaker in $\text{Fe}_{3-x}\text{C}@C-400$ compared with those in other samples, implying the limited carbon coating possibly ascribed to the insufficient CVD process under low temperature. The N_2 adsorption-desorption analysis (Figure 3b) was conducted to study the porous characters. All the samples show typical type II curves, confirming the hierarchical porosity of the $\text{Fe}_{3-x}\text{C}@C$ composites. The pore size distributions reveal the relatively concentrated pore size at range of 2 to 10 nm as shown in Figure 3c. Based on the Brunauer-Emmett-Teller (BET) calculation, the $\text{Fe}_{3-x}\text{C}@C-500$ exhibits the highest specific surface area of $196.9 \text{ m}^2 \text{ g}^{-1}$ compared with $\text{Fe}_{3-x}\text{C}@C-400$ ($124.2 \text{ m}^2 \text{ g}^{-1}$) and $\text{Fe}_{3-x}\text{C}@C-600$ ($80.2 \text{ m}^2 \text{ g}^{-1}$). The large surface area can facilitate sulfur homogenization and enhance physical sulfur confinement for shuttle inhibition.

The Fe content in $\text{Fe}_{3-x}\text{C}@C-400$, $\text{Fe}_{3-x}\text{C}@C-500$ and $\text{Fe}_{3-x}\text{C}@C-600$ samples (marked as D-1, D-2, D-3) was detected ≈ 87.4 , 81.2 , and $73.1 \text{ wt}\%$, respectively. Thus, the coating carbon content is accordingly 6.4 , 13.1 , $21.7 \text{ wt}\%$ (Figure 3d), indicating the intensified carbon coating along with the increase of temperature, which is consistent with the XRD and TEM analysis. The XPS spectra were collected to further study the surface compositions and chemical states of the $\text{Fe}_{3-x}\text{C}@C$ microspheres (Figure 3e). The high-resolution Fe 2p XPS spectra can be separated into two pairs of peaks for Fe^{3+} (713.0 and 726.9 eV) and Fe^{2+} (710.7 and 724.3 eV), and two pairs of satellite peaks (719.1 and 733.7 eV). It is noteworthy that the peak area ratio of Fe^{3+} to Fe^{2+} (I_3/I_2) varies with the temperature, suggesting the increased Fe deficiency in Fe_{3-x}C . This defective feature of $\text{Fe}_{3-x}\text{C}@C$ microspheres was further confirmed by electron paramagnetic resonance (EPR) as shown in Figure 3f. Distinctive EPR signals can be detected at $\approx 3510 \text{ G}$, verifying the existence of Fe-vacancies.^[28] Meanwhile, the intensification of EPR signal along with the increase of annealing temperature signifies the increase of defect content in the product, where the Fe deficiency increases the overall Fe

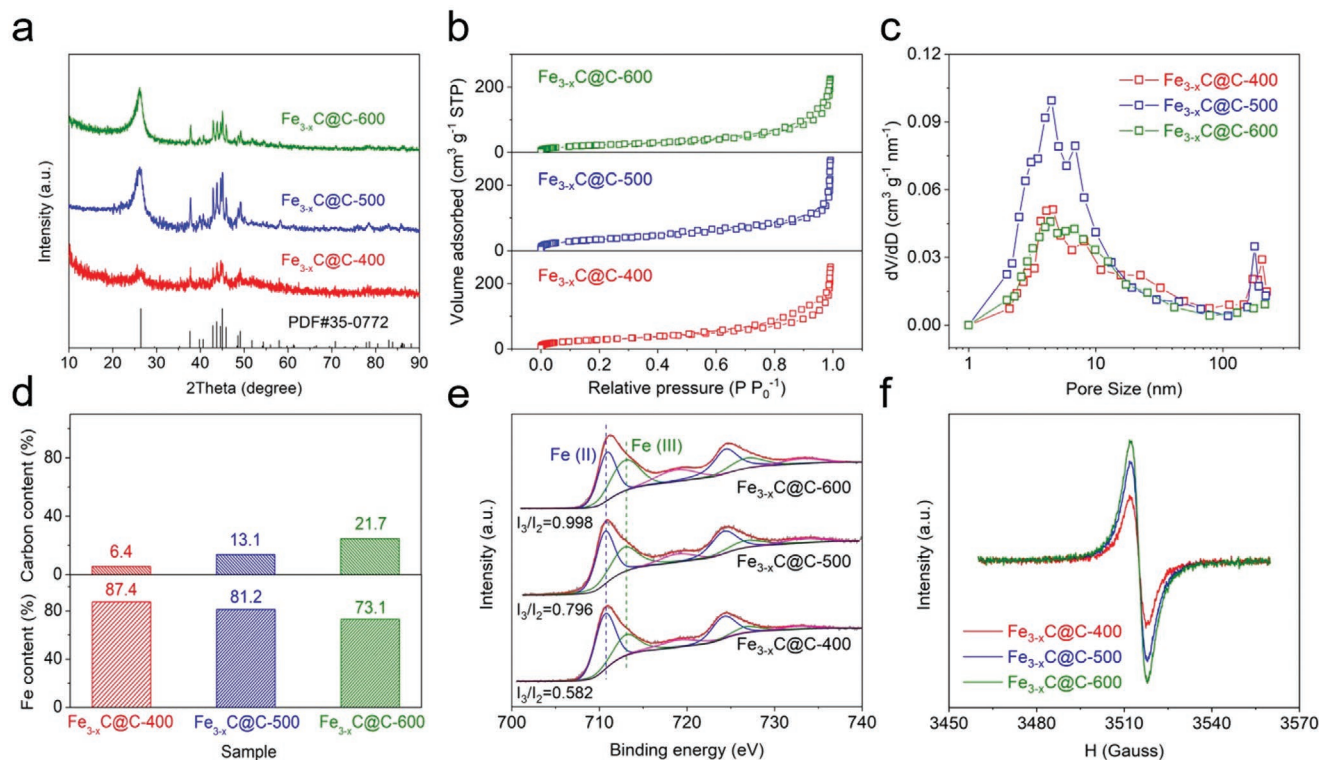


Figure 3. Structural and chemical analysis of $\text{Fe}_{3-x}\text{C}@C-400$, $\text{Fe}_{3-x}\text{C}@C-500$ and $\text{Fe}_{3-x}\text{C}@C-600$: a) XRD patterns, b) isotherm curves, c) BJH pore size distributions, d) carbon content and Fe content, e) high resolution Fe 2p XPS spectra, and f) EPR spectra.

valence state as well as the concentration of unpaired electrons in d-orbital.

To investigate the practical effect of the obtained $\text{Fe}_{3-x}\text{C}@C$ as sulfur host, the sulfur-contained composites ($\text{S}/\text{Fe}_{3-x}\text{C}@C-400$, $\text{S}/\text{Fe}_{3-x}\text{C}@C-500$ and $\text{S}/\text{Fe}_{3-x}\text{C}@C-600$) were prepared via melt-impregnation process (see details in Experimental section). The sulfur content in $\text{S}/\text{Fe}_{3-x}\text{C}@C-500$ was determined ≈ 74 wt% by the thermal gravimetric analysis (TGA) as shown in Figure S5 (Supporting Information). This can be attributed to the hollow microstructure of the $\text{Fe}_{3-x}\text{C}@C-500$, which provides sufficient space for sulfur accommodation. **Figure 4a** shows the CV curves of $\text{S}/\text{Fe}_{3-x}\text{C}@C-500$ electrode during the first three cycles at a scanning rate of 0.1 mV s^{-1} . The result shows two major reduction peaks at around 2.3 and 2.05 V, corresponding to the reduction of S_8 to soluble long-chain LiPS intermediates (Li_2S_n , $4 \leq n \leq 8$), and their further reduction into insoluble $\text{Li}_2\text{S}_2/\text{Li}_2\text{S}$, respectively. Meanwhile, the oxidation peaks at 2.3–2.4 V suggest the transformation of LiPS backs into elemental sulfur. The CV profile maintains well during the initial cycles, demonstrating the good reversibility of the sulfur reactions. Moreover, the charge–discharge curves of the $\text{S}/\text{Fe}_{3-x}\text{C}@C-500$ electrode at different cycles under 0.2 C are shown in Figure 4b. The galvanostatic cycling profiles perform two discharge plateaus and a charging slope, which corresponds well with CV results according to the multistep sulfur reaction mechanism. The voltage profile can be also sustained over 100 cycles with a stabilized capacity of 1089 mAh g^{-1} , indicating the excellent reaction kinetics and cycling stability. Furthermore, the $\text{S}/\text{Fe}_{3-x}\text{C}@C-500$ electrode preserves a small potential hysteresis over 100 cycles,

indicating limited LiPS shuttling and stabilized sulfur reaction kinetics. Figure 4c shows the charge-discharge profiles of the $\text{S}/\text{Fe}_{3-x}\text{C}@C-500$ electrode under different current densities. With the increase of the current rate, the potential gap between the charge and discharge plateaus increases gradually. However, the two distinctive discharge plateaus can be still obtained even at a high current density of 5 C, further confirming the excellent sulfur reaction kinetics in $\text{S}/\text{Fe}_{3-x}\text{C}@C-500$ electrode. The cyclic stabilities of different $\text{S}/\text{Fe}_{3-x}\text{C}@C$ electrodes were examined through galvanostatic cycling as shown in Figure 4d. In comparison, the $\text{S}/\text{Fe}_{3-x}\text{C}@C-500$ electrode exhibits the best cycling stability, delivering the highest capacity retention of 85.6% compared with those of the $\text{S}/\text{Fe}_{3-x}\text{C}@C-400$ (74.6%) and $\text{S}/\text{Fe}_{3-x}\text{C}@C-600$ (66.1%) electrode after 100 cycles at 0.2 C. Moreover, the rate performances of different $\text{S}/\text{Fe}_{3-x}\text{C}@C$ electrodes were also studied as shown in Figure 4e. Clearly, $\text{S}/\text{Fe}_{3-x}\text{C}@C-500$ electrode shows the best rate capability with discharge capacity of 1265, 992, 834, 700, and 609 mAh g^{-1} at the current density of 0.2 C, 0.5 C, 1 C, 2 C and 5 C, respectively, which are much higher than other $\text{S}/\text{Fe}_{3-x}\text{C}@C$ electrodes, demonstrating the obviously improved sulfur utilization. Meanwhile, the electrochemical impedance spectroscopy (EIS) spectra also reveals its low charge-transfer resistance (Figure 4f), indicating the favorable improvement of the electron/ion transfer because of the V_{Fe} -rich $\text{Fe}_{3-x}\text{C}@C$ architecture. These results strongly demonstrate the effectively catalyzed sulfur redox reactions by $\text{Fe}_{3-x}\text{C}@C-500$. Furthermore, the long-term cyclability of different $\text{S}/\text{Fe}_{3-x}\text{C}@C$ electrodes was explored as shown in Figure 4g. It can be clearly observed

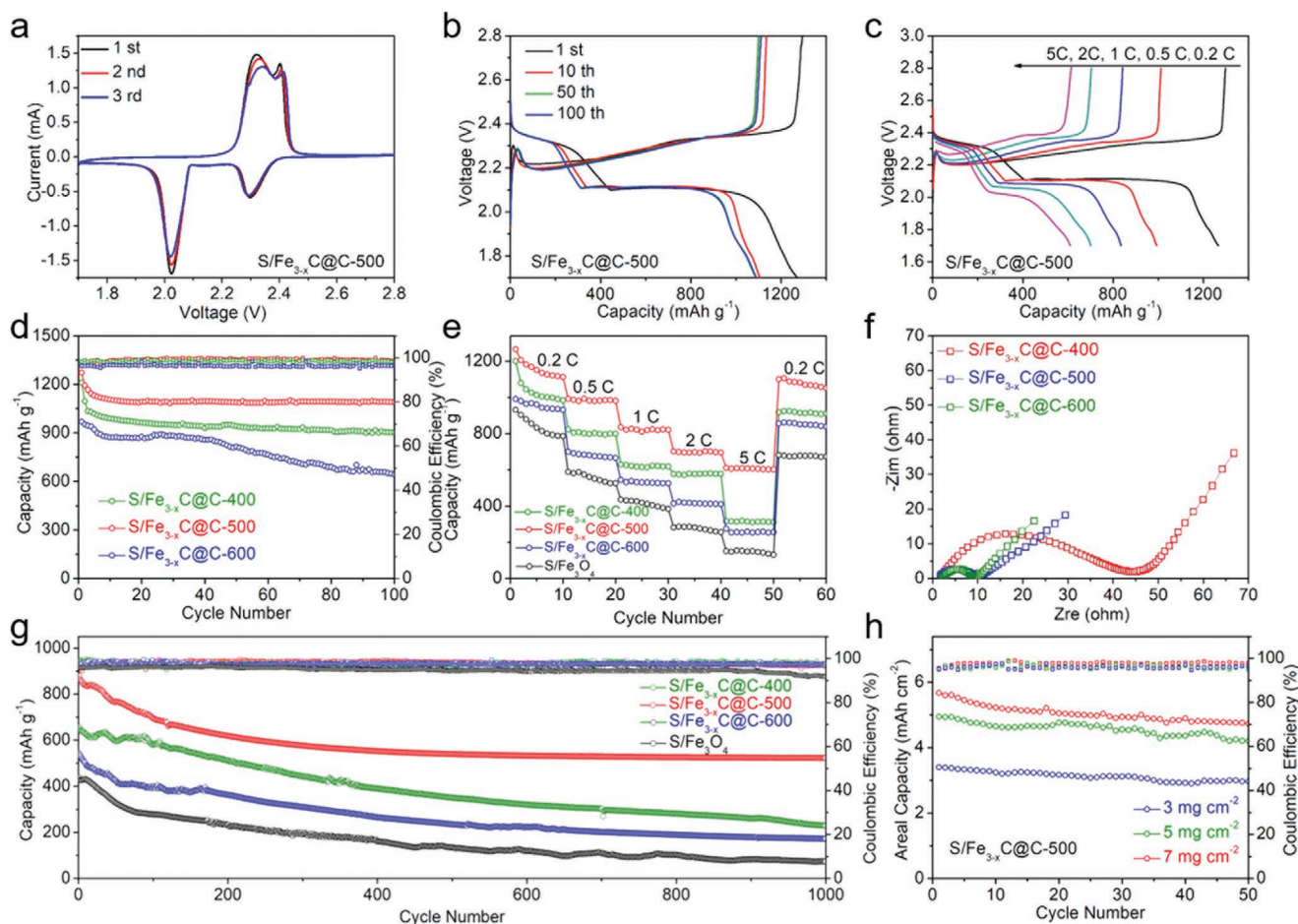


Figure 4. Electrochemical performance of different electrodes: a) CV curves, b,c) galvanostatic charge–discharge curves, d) cycling performance at 0.2 C, e) rate performance, f) EIS spectra, g) long-term cycling performance at 1 C, and h) high-loading cycling performances at 0.1 C.

that the $S/Fe_{3-x}C@C-500$ electrode delivers a much higher cycling stability with a high capacity retention over 60.3% after 1000 cycles compared with those of $S/Fe_{3-x}C@C-400$ (35.6%) and $S/Fe_{3-x}C@C-600$ electrode (31.9%). Meanwhile, $S/Fe_{3-x}C@C-500$ electrode also exhibits a high and steady coulombic efficiency over 99% upon the cycling, suggesting its effective inhibition on LiPS shuttling. For comparison, the rate performance and long-term cycling performance at 1 C of S/Fe_3O_4 electrodes are also shown in Figure 4e,g, which suffers from fast capacity fading along the increase of C-rate and the prolonged cycling, indicating its lack of sulfur confinement and sluggish reaction kinetics. Based on the above results, the reasons for the excellent electrochemical performance of $S/Fe_{3-x}C@C-500$ electrode can be described as follows: 1) the carbon coating and the highly porous hollow architecture enable the fast electron and ion transfers for facile sulfur redox reactions; 2) the uniformly distributed $Fe_{3-x}C$ nanoparticles in $Fe_{3-x}C@C-500$ fully exposes the active interfaces for their interactions with LiPS toward strong sulfur immobilization and efficient reaction catalysis. By contrast, the insufficient carbon coating in $S/Fe_{3-x}C@C-400$ and the agglomerated $Fe_{3-x}C$ particles in $S/Fe_{3-x}C@C-600$ fail to synergize these effects, thus suffering from the degraded electrochemical performance. Given this,

the $S/Fe_{3-x}C@C-500$ electrode was further explored with higher sulfur loadings in pursuit of higher energy density. Benefiting from the structural superiorities, the $Fe_{3-x}C@C-500$ enables a high areal capacity up to 5.6 mAh cm^{-2} under the raised sulfur loading up to 7 mg cm^{-2} with a decent cyclability as shown in Figure 4h.

In order to understand the underlying mechanism of the electrochemical improvements for $S/Fe_{3-x}C@C-500$ electrode, DFT calculations were performed with the optimized geometries of Li_2S_6 adsorption on ideal Fe_3C (031) and Fe-deficient $Fe_{3-x}C$ (031) surfaces as shown in Figure 5a. Clearly, Li_2S_6 exhibits a higher adsorption energy of -4.69 eV on $Fe_{3-x}C$ than that on Fe_3C surface (-3.82 eV), indicating the higher LiPS affinity of $Fe_{3-x}C$, which contributes to the stronger chemical sulfur immobilization and the resultant high-efficiency shuttle inhibition. Moreover, the Li_2S_6 adsorption on $Fe_{3-x}C$ (031) imposes an increased S–S bond length (2.36 \AA) compared with that on Fe_3C (031) surface (2.17 \AA), suggesting the easier breakage of the S–S bond and the facilitated sulfur redox reactions. Figure 5b depicts the density of states (DOS) patterns of Fe_3C and $Fe_{3-x}C$. A higher Fe d band center can be observed for $Fe_{3-x}C$ (-1.3573) compared with that of Fe_3C (-2.0939), suggesting that the existence of Fe vacancy tailors the Fe electronic structure and thereby enhancing the Li_2S_6

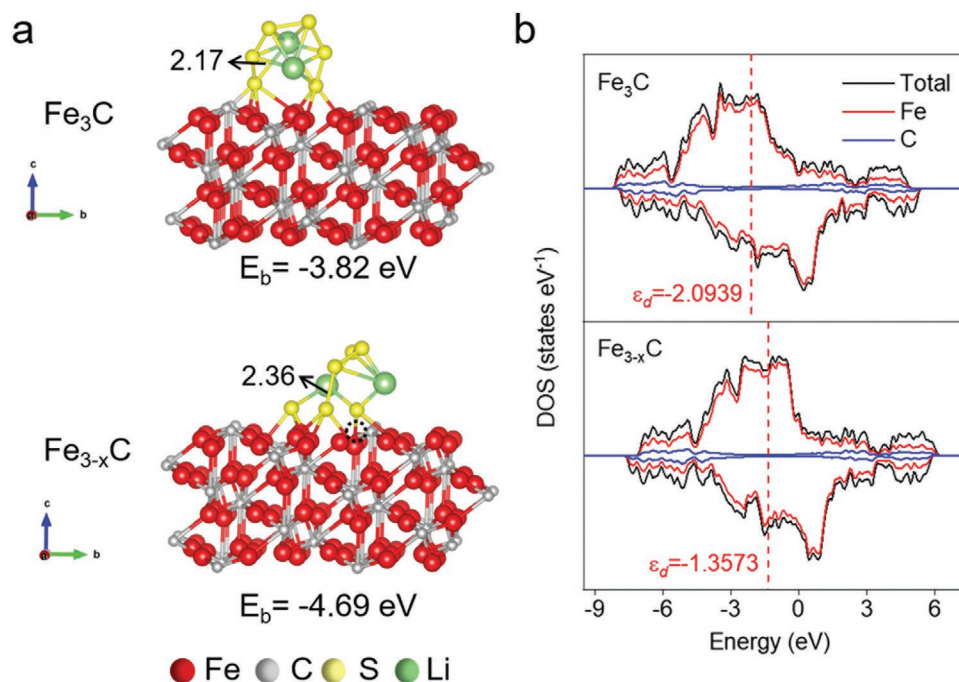


Figure 5. a) Geometrically stable configurations of Li₂S₆ adsorption on Fe₃C (031) and on Fe_{3-x}C (031) surfaces. b) DOS patterns of Fe₃C and Fe_{3-x}C.

adsorbability.^[29] Furthermore, the climbing-image nudged elastic band (CI-NEB) method was used to explore the kinetic process of Li₂S decomposition. The initial structure (IS), transition structure (TS), and final structure (FS) are shown in Figure S6 (Supporting Information). The Li₂S decomposition performs a much lower energy barrier of 0.51 eV on the V_{Fe}-rich Fe_{3-x}C than that on Fe₃C (1.72 eV), proving the facilitated Li₂S transformation kinetics by V_{Fe}.

The superior polysulfides adsorption of the Fe_{3-x}C@C-500 composite can be further visualized by immersing different composite materials in Li₂S₆/THF solution as shown in the inset of Figure 6a. Clearly, the Li₂S₆ solution gradually changes its color from dark brown to almost transparent after adsorption by Fe_{3-x}C@C-500. By contrast, much weakened Li₂S₆ absorption was observed for Fe_{3-x}C@C-400 and Fe_{3-x}C@C-600 ascribed to the lack of defects in Fe_{3-x}C@C-400, and the particle agglomeration in Fe_{3-x}C@C-600 that limit the overall amount of accessible adsorption sites. This difference can be also confirmed by the UV-vis spectroscopy as shown in Figure 6a. The absorption peaks at around 280 and 425 nm can be assigned to S₆²⁻ and S₄²⁻ species, respectively.^[30–33] The largest intensity decline of these peaks in Fe_{3-x}C@C-500 spectrum signifies the lowest LiPS concentration in the supernatant and verifies its strongest LiPS adsorbability. These results evidentially demonstrate that the Fe-deficiency and their efficient exposure are highly favorable for LiPS adsorption, which offers superior LiPS chemical confinement towards efficient shuttle inhibition.

The catalyzation effect on the redox reactions was further investigated. Symmetric cells were assembled based on identical Fe_{3-x}C@C electrodes and Li₂S₆ electrolyte for the kinetics study. Notably, the Fe_{3-x}C@C-500 exhibits two pairs of redox

peaks with the highest redox current response among the different samples, indicating its significantly faster and more sufficient LiPS conversions (Figure 6b). The CV profile of Fe_{3-x}C@C-500 symmetric cell well maintains upon several cycles (Figure 6c), suggesting the highly reversibility of LiPS oxidation/reduction process. In addition, the EIS spectra shows the low charge transfer resistance for the Fe_{3-x}C@C-500 (Figure 6d), further confirming the facile sulfur reactions in the according configuration. Apart from that, three-electrode linear sweep voltammetry (LSV) tests were performed to specifically study the Li₂S oxidation behavior on different catalytic surfaces (Figure 6e). The Fe_{3-x}C@C-500 electrode exhibits a considerably lower onset potential of -0.42 V compared with Fe_{3-x}C@C-400 (-0.34 V) and Fe_{3-x}C@C-600 (-0.38 V), indicating its lowest overpotential for Li₂S oxidation and the great kinetic enhancement. This result can be further supported by the Tafel plot as shown in Figure 6f, which reveals the smallest Tafel slope of 76 mV dec⁻¹ for Fe_{3-x}C@C-500, comparing with those of Fe_{3-x}C@C-400 (316 mV dec⁻¹) and Fe_{3-x}C@C-600 electrodes (176 mV dec⁻¹). The evidential improvement in sulfur reaction kinetics can be attributed to the hierarchical porous hollow microsphere architecture, which offers large surface area and vast active interfaces for uniformizing the sulfur distribution and reducing ion/electron transportation pathway. Beyond that, the enriched Fe-vacancies further empower abundant adsorption sites to promote the chemical interactions between Fe_{3-x}C@C and LiPS, as well as catalytic sites to accelerate the LiPS conversion reactions. As a result, the Fe_{3-x}C@C-500 hollow microspheres serve as highly effective sulfur immobilizer and promoter, contributing to expedite Li-S kinetics and enhanced cyclic stability.

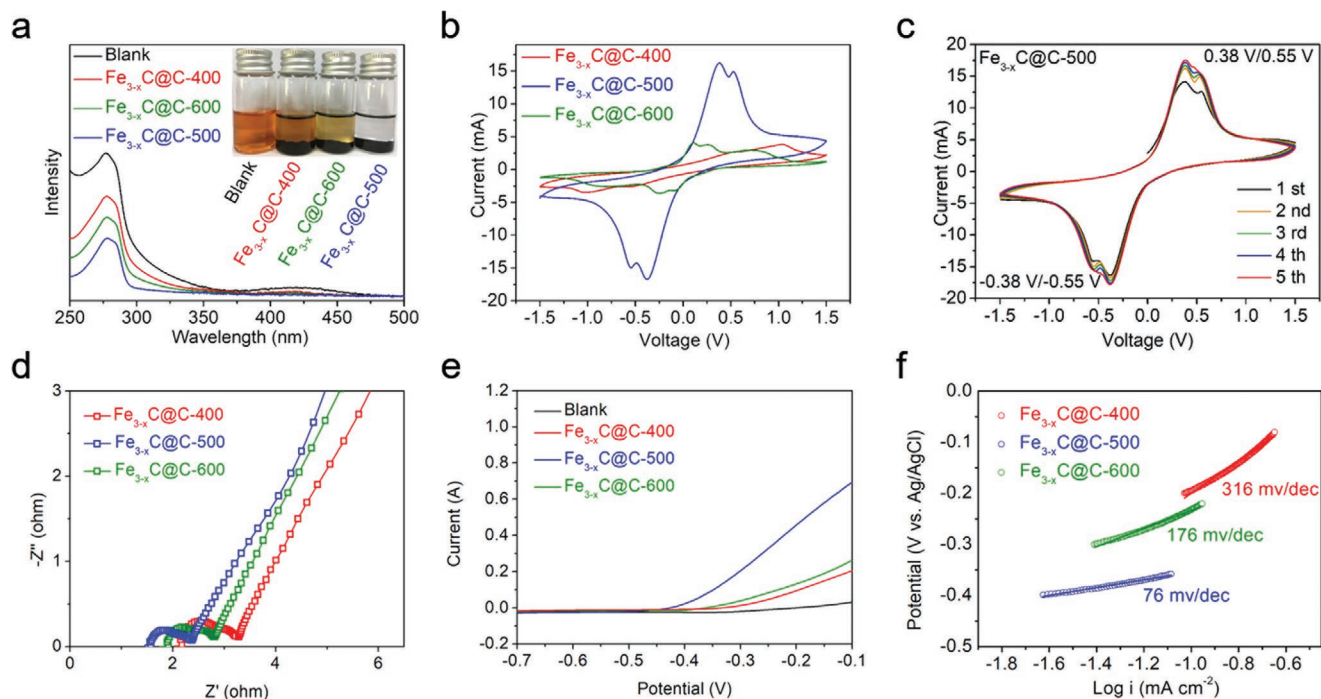


Figure 6. a) UV-vis spectra of Li_2S_6 solution before and after adsorbed by various materials (inset figure: optical images of Li_2S_6 adsorption test); b,c) CV curves and d) EIS spectra of Li_2S_6 symmetric cells with $\text{Fe}_{3-x}\text{C}@C$ electrodes; e) LSV curves and f) Tafel plots of Li_2S oxidation on different $\text{Fe}_{3-x}\text{C}@C$ surfaces.

3. Conclusion

We have developed the hierarchical $\text{Fe}_{3-x}\text{C}@C$ hollow microspheres consisting of Fe-deficient Fe_{3-x}C subunits with mesoporous carbon coating. The porous, hollow, and hierarchical architecture competently accommodates the volume expansion during sulfur lithiation, and meanwhile establishes highly ionic/electronic conductive network for efficient mass/charge transportation. More importantly, the defective Fe_{3-x}C acts as an excellent LiPS adsorbent to strongly immobilize the sulfur species against their shuttling behaviors, as well as efficient catalyst to promote the sulfur conversion reaction kinetics. Attributed to the structural superiorities, the Li-S cells based on the as-developed $\text{Fe}_{3-x}\text{C}@C$ exhibit high sulfur utilization, strong sulfur confinement, and fast sulfur conversions, leading to excellent electrochemical performance, i.e., high areal capacity of 5.6 mAh cm^{-2} , good rate capability up to 5 C, and remarkable cyclic stability over 1000 cycles with a low capacity fading rate of 0.04% per cycle at 1 C. This strategy offers a new route to design multifunctional sulfur immobilizer with highly adoptive and catalytic capabilities for rapid LPS adsorption-conversion process, holding a great promise in promoting the practical application of Li-S batteries as well as enlightening the material engineering in related energy storage and conversion areas.

4. Experimental Section

Synthesis of Fe_3O_4 Hollow Microspheres: 60 mL mixed solution of isopropanol and glycerol was first prepared in volume ratio of 7:1. Subsequently, $\text{Fe}(\text{NO}_3)_3 \cdot 6\text{H}_2\text{O}$ (0.5 mmol) was added to the mixed solution

and stirred for 5 min, followed by the addition of deionized water (1 mL) and further stirring for 10 min. The obtained solution was transferred to a stainless-steel autoclave and subjected to the thermal treatment at 190°C for 12 h. The product was collected by centrifugation, and washed by deionized water and absolute ethanol to remove impurity. After dried in 70°C , the precursor powder was calcined at 350°C for 12 h in N_2 with a heating rate of 1°C min^{-1} to yield the Fe_3O_4 hollow microsphere.

Synthesis of $\text{Fe}_{3-x}\text{C}@C$ Hollow Microspheres: $\text{Fe}_{3-x}\text{C}@C$ was prepared by a conventional CVD method. First, the prepared Fe_3O_4 powder was placed in a tube furnace and heated to 400, 500, or 600°C under Ar with a ramping rate of 1°C min^{-1} (denoted as $\text{Fe}_{3-x}\text{C}@C-400$, $\text{Fe}_{3-x}\text{C}@C-500$ and $\text{Fe}_{3-x}\text{C}@C-600$, respectively). Subsequently, acetylene and hydrogen were introduced for 5 min, wherein the flow rate of argon, hydrogen, and acetylene was 300, 200, and 100 mL min^{-1} respectively. The $\text{Fe}_{3-x}\text{C}@C$ hollow microspheres were collected after cooling to room temperature under Ar atmosphere.

Synthesis of S- $\text{Fe}_{3-x}\text{C}@C$ Composites: S- $\text{Fe}_{3-x}\text{C}@C$ composite was prepared by a melt-diffusion process. The prepared $\text{Fe}_{3-x}\text{C}@C$ and elemental sulfur were ground uniformly at a mass ratio of 1:3. Following calcination at 155°C for 6 h in Ar was performed to obtain the S- $\text{Fe}_{3-x}\text{C}@C$ composite.

Materials Characterization: XRD pattern was recorded with a Bruker D8 Advance X-ray diffractometer (XRD) to determine the crystallinity and composition of the sample. Scanning electron microscopy (SEM) and transmission electron microscopy (TEM) images were taken by Hitachi S-4800 and JEOL 2100, respectively. The specific surface area was calculated using the Brunauer-Emmett-Teller (BET) equation based on the N_2 adsorption-desorption measurement (V-Sorb 2800P). X-ray photoelectron spectroscopy (XPS, Thermo Fisher Scientific, ESCALAB 250Xi, America) was used to identify the surface chemical states. Thermal gravimetric analysis (TGA, TA Instruments, SDT Q-600) was performed at a heating rate of $10^\circ\text{C min}^{-1}$ under Ar atmosphere.

Electrochemical Characterization: The cathode slurry was prepared by mixing 80 wt% S- $\text{Fe}_{3-x}\text{C}@C$ composite, 10 wt% PVDF binder, and 10 wt% carbon black in NMP dispersant solvent. The slurry was cast on carbon coated aluminum foil and dried at 60°C for 12 h. Bis-(trifluoromethanesulfonyl) imide (LiTFSI, 1.0 M) with LiNO_3 (0.1 M)

dissolved in 1,3-dioxolane (DOL) and 1,2-dimethoxyethane (DME) (v/v, 1:1) was used as electrolyte. CR2032 coin cells were assembled with S-Fe_{3-x}C@C composite cathode, polypropylene separator (Celgard) and lithium foil anode in an argon-filled glove-box (Ar > 99.9%). The charge–discharge cycling was conducted by Neware (Shenzhen, China) tester within the voltage range of 1.7 to 2.8 V versus Li⁺/Li. Versa STAT4 (Princeton Applied Research) was used to perform cyclic voltammetry (CV) at a scanning rate of 0.1 mV s⁻¹ and electrochemical impedance spectroscopy (EIS) from 100 kHz to 0.01 Hz.

Density Functional Theory Calculations: The density functional theory (DFT) calculations were performed using the Vienna Ab initio Simulation Package (VASP) with Perdew–Burke–Ernzerhof (PBE) for the exchange and correlation energy terms. The Fe₃C (031) surface was chosen for the calculation. The Fe-deficient Fe_{3-x}C (031) surface was built by removing one Fe atom from intact Fe₃C surface. A 2 × 1 supercell and Monkhorst–Pack 2 × 2 × 1 grid in k-space were used. The plane-wave cutoff energy was 400 eV and the vacuum height was 15 Å. The adsorption energies (E_{ads}) of Li₂S₆ on Fe₃C (031) and Fe_{3-x}C (031) surface were calculated.

Preparation of Li₂S₆ Electrolyte: Li₂S and sulfur were mixed at a molar ratio of 1:5 in conventional electrolyte in a glass bottle. The mixture was magnetic stirred for 24 h at 50 °C in Ar-filled glove box to obtain a Li₂S₆ electrolyte (0.2 M) the symmetric cell characterizations. In addition, Li₂S₆ electrolyte (5 × 10⁻³ M) was prepared through the same method for the adsorption test.

Symmetric Cells Assembly and Measurement: The electrodes for symmetric cells were prepared by mixing actively materials and PVDF binder at a weight ratio of 9:1 in NMP to obtained slurry, which was then coated on carbon cloth with a mass loading of 1.2 mg cm⁻². The punched electrode disks (12 mm) were used as identical working and counter electrodes to assemble symmetric cells with Li₂S₆ electrolyte (75 μL). The CV curves were measured on electrochemical workstation (Chenhua CHI-660C) at a scanning rate of 10 mV s⁻¹ from -1.5 to 1.5 V. EIS spectra were also collected in electrochemical workstation (Princeton Applied Research Versa STAT4) within the frequency range of 100 kHz to 0.1 Hz.

Linear Sweep Voltammetry Measurement: Three-electrode linear sweep voltammetry (LSV) tests were performed to evaluate the catalytic activity of Fe_{3-x}C@C composites. The cells consisted of Fe_{3-x}C@C composites as the working electrode, saturated Ag/AgCl electrode as reference, platinum sheet as counter electrode, and Li₂S/methanol solution (0.1 M) as electrolyte. For the Fe_{3-x}C@C electrode preparation, the slurry containing Fe_{3-x}C@C composites and PVDF at a weight ratio of 5:1 was coated on bare glass carbon. The LSV measurements were conducted using electrochemical workstation (Princeton Applied Research Versa STAT4) at a scanning rate of 5 mV s⁻¹ from -0.7 to -0.1 V.

Supporting Information

Supporting Information is available from the Wiley Online Library or from the author.

Acknowledgements

Y.Z. and G.L. contributed equally to this work. This research was funded by the National Natural Science Foundation of China Program (No. U1909213), Xijiang R&D Team (X.W.), Guangdong Innovative and Entrepreneurial Team Program (No. 2016ZT06C517), Science and Technology Program of Guangzhou (No. 2019050001), the Program for the Outstanding Young Talents of Hebei Province, and Chunhui Project of Ministry of Education of the People's Republic of China (Grant No. Z2017010). The authors also thank the support from Natural Sciences and Engineering Research Council of Canada, University of Waterloo, and Waterloo Institute for Nanotechnology.

Conflict of Interest

The authors declare no conflict of interest.

Keywords

cathode materials, electrochemical performance, Fe vacancies, iron carbide, lithium–sulfur batteries

Received: February 7, 2020

Revised: March 2, 2020

Published online: April 9, 2020

- [1] L. Kong, B. Q. Li, H. J. Peng, R. Zhang, J. Xie, J. Q. Huang, *Adv. Energy Mater.* **2018**, *8*, 1800849.
- [2] J. Lu, Z. W. Chen, F. Pan, Y. Cui, K. Amine, *Electrochem. Energy Rev.* **2018**, *1*, 35.
- [3] Y. Pang, J. S. Wei, Y. G. Wang, Y. Y. Xia, *Adv. Energy Mater.* **2018**, *8*, 1702288.
- [4] X. Li, M. Bani, A. Lushington, X. F. Yang, Q. Sun, Y. Zhao, C. Q. Liu, Q. Z. Li, B. Q. Wang, W. Xiao, C. H. Wang, M. S. Li, J. W. Liang, R. Y. Li, Y. F. Hu, L. Goncharova, H. M. Zhang, T. K. Sham, X. L. Sun, *Nat. Commun.* **2018**, *9*, 4509.
- [5] S. H. Liu, J. Li, X. Yan, Q. F. Su, Y. H. Lu, J. S. Qiu, *Adv. Mater.* **2018**, *30*, 1706895.
- [6] S. Gu, C. Z. Sun, D. Xu, Y. Lu, J. Jin, Z. Y. Wen, *Electrochem. Energy Rev.* **2018**, *1*, 599.
- [7] G. Li, X. L. Wang, M. H. Seo, M. Li, L. Ma, Y. F. Yuan, *Nat. Commun.* **2018**, *9*, 705.
- [8] S. H. Chung, A. Manthiram, *Adv. Mater.* **2018**, *30*, 1705951.
- [9] Y. R. Zhong, L. C. Yin, P. He, W. Liu, Z. S. Wu, H. L. Wang, *J. Am. Chem. Soc.* **2018**, *140*, 1455.
- [10] J. Zhang, G. P. Jiang, T. Cumberland, P. Xu, Y. L. Wu, S. Delaet, A. P. Yu, Z. W. Chen, *InfoMat* **2019**, *1*, 234.
- [11] G. R. Li, S. Wang, Y. N. Zhang, M. Li, Z. W. Chen, J. Lu, *Adv. Mater.* **2018**, *30*, 1705590.
- [12] J. H. Zhang, M. Huang, B. J. Xi, K. Mi, A. H. Yuan, S. L. Xiong, *Adv. Energy Mater.* **2018**, *8*, 1701330.
- [13] W. L. Cai, G. R. Li, K. L. Zhang, G. N. Xiao, C. Wang, K. F. Ye, *Adv. Funct. Mater.* **2018**, *28*, 1704865.
- [14] D. Gueon, J. T. Hwang, S. B. Yang, E. Cho, K. Sohn, D. K. Yang, *ACS Nano* **2018**, *12*, 226.
- [15] R. P. Fang, K. Chen, L. C. Yin, Z. H. Sun, F. Li, H. M. Cheng, *Adv. Mater.* **2019**, *31*, 1800863.
- [16] Z. L. Xu, J. K. Kim, K. Kang, *Nano Today* **2018**, *19*, 84.
- [17] D. H. Liu, C. Zhang, G. M. Zhou, W. Lv, G. W. Ling, L. J. Zhi, *Adv. Sci.* **2018**, *5*, 1700270.
- [18] H. J. Peng, J. Q. Huang, X. B. Cheng, Q. Zhang, *Adv. Energy Mater.* **2017**, *7*, 1700260.
- [19] J. R. He, L. Luo, Y. F. Chen, A. Manthiram, *Adv. Mater.* **2017**, *29*, 1702707.
- [20] T. Chen, Z. W. Zhang, B. R. Cheng, R. P. Chen, Y. Hu, L. B. Ma, *J. Am. Chem. Soc.* **2017**, *139*, 12710.
- [21] C. Ye, L. Zhang, C. X. Guo, D. D. Li, A. Vasileff, H. H. Wang, *Adv. Funct. Mater.* **2017**, *27*, 1702524.
- [22] T. Chen, L. B. Ma, B. R. Cheng, R. P. Chen, Y. Hu, G. Y. Zhu, *Nano Energy* **2017**, *38*, 239.
- [23] Z. Y. Li, Q. M. Gao, X. Liang, H. Zhang, H. Xiao, P. Xu, *Carbon* **2019**, *150*, 93.
- [24] Q. Y. Hao, G. L. Cui, Y. G. Zhang, J. D. Li, Z. S. Zhang, *Chem. Eng. J.* **2020**, *381*, 122672.
- [25] H. P. Li, J. Y. Wang, Y. G. Zhang, Y. Wang, A. Mentbayeva, Z. Bakenov, *J. Power Sources* **2019**, *437*, 226901.
- [26] E. Salhab, J. L. Zhao, J. Y. Wang, M. Yang, B. Wang, D. Wang, *Angew. Chem., Int. Ed.* **2019**, *58*, 9078.
- [27] D. T. Kuang, L. Z. Hou, S. L. Wang, H. Luo, L. W. Deng, J. He, M. Song, *Appl. Surf. Sci.* **2019**, *493*, 1083.

- [28] K. Y. Zhu, T. Wu, M. R. Li, R. F. Lu, X. F. Zhu, W. S. Yang, *J. Mater. Chem. A* **2017**, *5*, 19836.
- [29] C. Ye, Y. Jiao, H. Y. Jin, A. D. Slattery, *Angew. Chem., Int. Ed.* **2018**, *57*, 16703.
- [30] D. Luo, G. R. Li, Y. P. Deng, Z. Zhang, *Adv. Energy Mater.* **2019**, *9*, 1900228.
- [31] J. F. Zhang, G. R. Li, Y. G. Zhang, W. Zhang, X. Wang, Y. Zhao, J. D. Li, Z. W. Chen, *Nano Energy* **2019**, *64*, 103905.
- [32] Y. Tian, G. R. Li, Y. G. Zhang, D. Luo, X. Wang, Y. Zhao, H. Liu, P. G. Ji, X. H. Du, J. D. Li, Z. W. Chen, *Adv. Mater.* **2019**, 1904876.
- [33] Y. Tian, Y. Zhao, Y. G. Zhang, L. Ricardez-Sandoval, X. Wang, J. D. Li, *ACS Appl. Mater. Interfaces* **2019**, *11*, 23271.